energies

MDPI

Article

Very Short-Term Forecast: Different Classification Methods of the Whole Sky Camera Images for Sudden PV Power Variations Detection

Alessandro Niccolai *, Emanuele Ogliari, Alfredo Nespoli, Riccardo Zich and Valentina Vanetti

Department of Energy, Politecnico di Milano, Via Giuseppe La Masa, 34, 20156 Milan, Italy
* Correspondence: alessandro.niccolai@polimi.it

Abstract: Solar radiation is by nature intermittent and influenced by many factors such as latitude, season and atmospheric conditions. As a consequence, the growing penetration of Photovoltaic (PV) systems into the electricity network implies significant problems of stability, reliability and scheduling of power grid operation. Concerning the very short-term PV power production, the power fluctuations are primarily related to the interaction between solar irradiance and cloud cover. In small-scale systems such as microgrids, the adoption of a forecasting tool is a brilliant solution to minimize PV power curtailment and limit the installed energy storage capacity. In the present work, two different nowcasting methods are applied to classify the solar attenuation due to clouds presence on five different forecast horizons, from 1 to 5 min: a Pattern Recognition Neural Network and a Random Forest model. The proposed methods are tested and compared on a real case study: available data consists of historical irradiance measurements and infrared sky images collected in a real PV facility, the SolarTech^{LAB} in Politecnico di Milano. The classification output is a range of values corresponding to the future value assumed by the Clear Sky Index (CSI), an indicator allowing to account for irradiance variations only related to clouds passage, neglecting diurnal and seasonal influences. The developed models present similar performance in all the considered time horizons, reliably detecting the CSI drops caused by incoming overcast and partially cloudy sky conditions.

Keywords: clear sky index; random forest; pattern recognition neural network; nowcasting; all-sky-cam

check for updates

Citation: Niccolai, A.; Ogliari, E.; Nespoli, A.; Zich, R.; Vanetti, V. Very Short-Term Forecast: Different Classification Methods of the Whole Sky Camera Images for Sudden PV Power Variations Detection. *Energies* **2022**, *15*, 9433. https://doi.org/10.3390/en15249433

Academic Editor: Peng Kou

Received: 1 November 2022
Accepted: 8 December 2022
Published: 13 December 2022

1. Introduction

In recent years, the share of renewables in the energy mix has been growing worldwide [1] in order to address the increasing energy demand and due to the necessity of reduce the greenhouse gases emissions caused by conventional power production systems [2,3]. However, concerning the solar source, a large integration of photovoltaic (PV) power into electricity grids is challenging [4], as solar radiation is heavily dependent on several factors such as latitude, season, atmosphere and ambient conditions; hence, it often fluctuates erratically [5]. This leads to a decrease in stability and reliability of the power system, with inefficient utilities planning and consequent financial losses [6]. The large-scale penetration of PV installations into the grid is hindered by this uncontrollable variability of radiation at ground level: since PV generation is strongly correlated with the solar irradiation incident on PV modules, the intrinsic variability of solar radiation reflects on to the variability of PV power production [7]. In more detail, the solar power fluctuations are primarily related to two aspects: the first one is the inherent radiation variation due to the diurnal pattern, which is determined by rotation and revolution of the Earth; the second one is related to the changes in meteorological conditions, such as the coverage given by clouds [8]. Due to a very short-term time horizon, the sudden variations of solar irradiance are primarily caused by the clouds' passage [9].

In small-scale plants, such as microgrids, the PV power fluctuations linked to the variability of the solar source are commonly managed by exploiting the active power reduction capacity of the inverter to limit production peaks. An additional approach is the exploitation of energy storage system with the function of supplying energy during power declines and to store energy during power peaks [10]. In minute scale time horizon, batteries can be used to smooth the power profile by properly setting the discharging and the charging phases [11]. Effective management of these systems can be achieved through their integration with forecasting tools that allow predicting the occurrence of such fluctuations [12]: this allows the battery to charge and discharge earlier, resulting in less energy capacity required and therefore lower costs [13].

Forecasting at minute scale commonly exploits cloud motion vectors obtained through sky cameras, satellite images or ground-based sensors [14]. Among these possibilities, the use of sky camera has been proven to be the most suitable thanks to its temporal and spatial resolution [15]. Indeed, it can provide advanced warning of approaching clouds at a lead time from few minutes to hours in a range of few kilometres [16]. Moreover, its combination with a solar radiation sensor enables to uncover the effect of specific types of clouds on the radiation [17].

In scientific literature, several irradiance forecast and classification approaches exploit whole-sky cameras to acquire sky images and then perform analyses to specific groups of pixels or Regions Of Interest (ROI) of an image, such as in the sun's surrounding or upwind. The features extracted can be categorized as either spectral (related to statistical properties of pixel groups, e.g., mean, standard deviation), textural (i.e., contrast, homogeneity, entropy) or color-related (saturation, hue) [18]. Concerning spectral features, they allow to evaluate the general weather condition, e.g., clear or cloudy sky [19], and they play a crucial role in the accuracy of cloud classification results [18]. Another approach using a whole-sky imager consists of providing directly the images to a deep learning model [20], that is a more complex method with high accuracy, but which requires large dataset to be implemented. Other techniques quantify or predict the solar variability through some indexes, and not directly the solar irradiance. For instance, the cloud coverage prediction is implemented in [21] using an artificial neural network and the temporal variability of solar irradiance is classified in [7] through the use of clear sky index.

The present work, in line with a previous one [22], aims at developing a nowcasting model capable of being integrated with the control strategy of batteries and able to predict, over different time horizons ranging from 1 to 5 min, the occurrence of PV power fluctuations. Such a tool allows to get early alerts on both sudden increases and sharp decreases in solar irradiance and, consequently, in PV production. The tool exploits, as inputs, infrared images acquired through a whole-sky camera and meteorological measurements recorded by a properly equipped weather station: the combined exploitation of these types of information in the nowcasting of solar irradiance fluctuations constitutes the novelty of the present work. Many machine learning techniques have been proposed in scientific literature to classify and predict irradiance: specifically, Artificial Neural Networks (ANN) and Random Forest (RF) models are deemed to be among the most promising ones [23,24].

With respect to other research papers that exploit all-sky camera images, the method implemented here requires a lower number of images for achieving good results with a lower number of images. The use of machine learning methods overcome the need of a specific cloud modeling that requires much information that are hard to be estimated or calculated.

2. Procedure

The present section discusses the selected classification models, the structure of available data and the performance metrics adopted to assess the classification accuracy.

2.1. Tested Methodologies

In this work, different methods are tested to detect the occurrence of sudden PV power fluctuations, employing Artificial Neural Network (ANN) and Random Forest (RF). An ANN is a Machine Learning tool that mimics the structure and the learning mechanism typical of the human brain. Its structure is conceptually divided into three blocks: one input layer, one or more hidden layers and one output layer [25]. The input layer is responsible of receiving the inputs from outside the network. Then, the signal flows into the hidden layers, where it is processed by the hidden neurons. Lastly, the output layer has the function of predicting the final result, starting from the information received from the previous layers [26]. An ANN is capable of recognizing hidden patterns between input data and a series of output classes, thus acting as classifier.

The ANN developed in the present study is characterized by a feed-forward network architecture. The dimension of the hidden layers, i.e., the number of hidden neurons, is selected through a sensitivity analysis aimed at finding the optimal compromise between model performance and complexity. In practical terms, this procedure allows to select the desired structure by analyzing the classification performance in function of the model structure exploiting the cross-entropy metric [27]. During the training phase of the ANN, 70% of the available data are used as training set, 10% as validation set and 20% as test set. The training is performed through the scaled conjugate gradient back-propagation algorithm.

On the other hand, the RF is an ensemble method composed by several Decision Tree classifiers as base learners. Each base learner performs predictions through a sequence of binary partitions, the so-called "splits", on input variables: each sample, when processed, starts from the "root node" of the tree and flows across its structure until it reaches a "leaf node", representing an output class. The classification outputs of all the base learners are then properly aggregated in order to obtain the final RF output [28]. The RF structure allows to avoid overfitting issues and to effectively handle noisy data. During the training phase, each tree is trained using a randomly selected subset of available data, relying on the idea of bagging [29]. Some samples may be used to train several decision trees, while other samples may never be involved in the training procedure. The latter samples are called "Out-Of-Bag" (OOB) samples and, being completely extraneous to the training process, they are useful to assess the RF classification performance.

As for the ANN model, a proper sizing of the RF structure is achieved through a sensitivity analysis procedure, aimed once again at finding a reasonable compromise between complexity and classification accuracy. This time, the sizing is based on the OOB samples and allows to select a proper number of trees involved in the classification task.

2.2. Available Data

All methods are tested, validated and compared on a real case study: a PV facility at SolarTech$^{\text{LAB}}$, on the rooftop of the Department of Energy at Politecnico di Milano, Milan, Italy (Figure 1).

Figure 1. SolarTech$^{\text{LAB}}$ PV facility at Politecnico di Milano, Italy.

The available data, corresponding to 72 days comprised between September 2019 and March 2020 and recorded with a time granularity of one minute, are collected by means of sensors installed in a dedicated weather station and a whole-sky camera placed in the proximity of the considered PV plant. In more detail, the Global Horizontal Irradiance (GHI) measurements are acquired through an irradiance sensor, while images in the infrared spectral region are collected through the all-sky camera.

The weather conditions are monitored with a meteorological station equipped with different sensors to record several ambient parameters: solar irradiance, temperature, humidity, wind speed, wind direction and rain collector. Solar irradiance is measured with two secondary standard pyranometers for the measurement of the total (or global) irradiance on the horizontal and 30° tilt planes. In addition, a pyranometer with shadow band is available for measuring the diffuse solar irradiance. The pyranometer at 30° tilt is directly used to define the solar irradiation on the PV modules which have the same tilt. The main characteristics of the sensors together with the temperature measuring equipment are shown in Figure 2 on the right and reported in Table 1. The meteorological station performs ambient conditions measurements every ten seconds. The average, maximum, minimum and the standard deviation of these values measured by the above-mentioned sensors are calculated every minute and they are stored into a database.

The employed Sky InSight^{TM} is a patented infrared all-sky imager for the continuous tracking and forecasting of the cloud cover developed by Reuniwatt [30].

A schematic representation of the adopted all-sky camera is reported in Figure 2 on the right. The infrared camera films an underlying hemispherical mirror, observing the cloud ceiling with a 360° angle corresponding to a 2 km radius. The use of the infrared vision technology allows a noticeable accuracy for day and night cloud detection, offering many advantages in comparison to optical cameras:

- It avoids segmentation errors related to the "circumsolar", i.e., the overexposure region surrounding the sun.
- It allows steady performance in conditions such as dawn, sunset, storms, etc. by overcoming optical brightness and contrast variation issues.
- It is capable to provide information such as altitude and optical thickness of clouds.

Table 1. Solar irradiance and temperature sensor characteristics.

Irradiance Sensors	**Pyranometer (LSI, DPA252)**
Standard	Secondary standard ISO 9060
Measurements range (W/m^2)	<2000
Spectral range	300–3000 nm
Total achievable daily uncertainty	<2%
Directional response	<±5.4 W/m^2
Thermal drift	<2%
Temperature and humidity sensor (LSI, DMA 875)	
Temperature sensor	Pt100 1/3 B (DIN EN 60751)
Measurements range	[−30 °C, +70 °C]
Uncertainty	0.2 °C (at 0 °C)
Resolution	0.04 °C
Response time (T90)	3 min: with filter; 20 s: without filter (air speed 0.2 m/s)

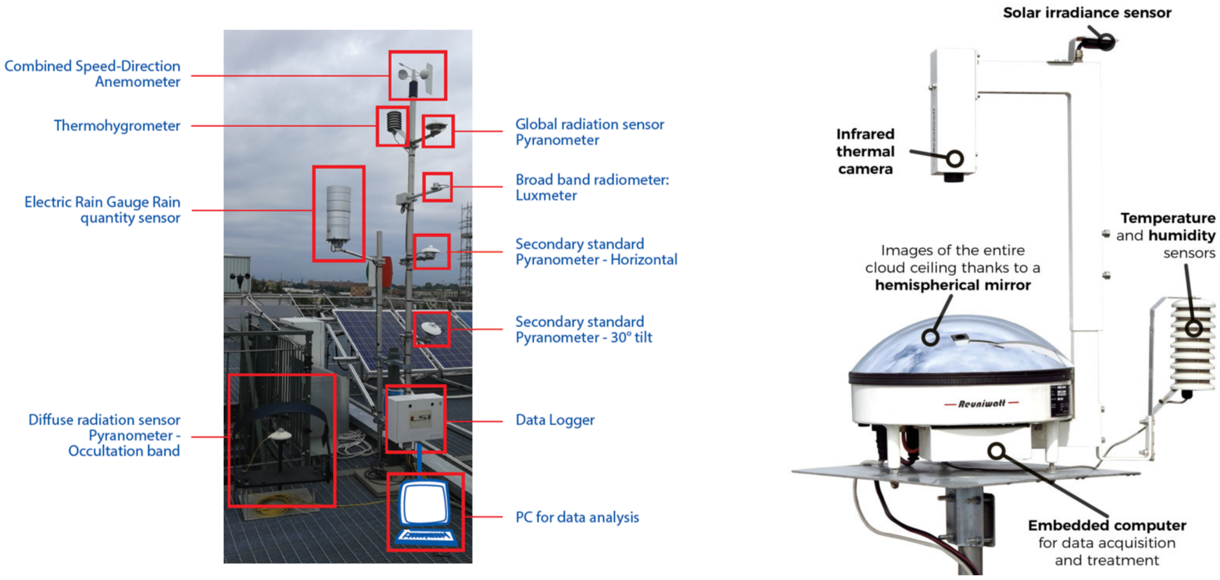

Figure 2. Weather station sensors (**left**) and 3D scheme of a whole-sky camera (**right**).

Figure 3 shows an example of infrared image acquired with the described system: the blue part corresponds to the clear sky, the clouds are represented by different shades of color and the sun is indicated by a black dot. The central red area and the surroundings are part of the whole-sky camera structure [31].

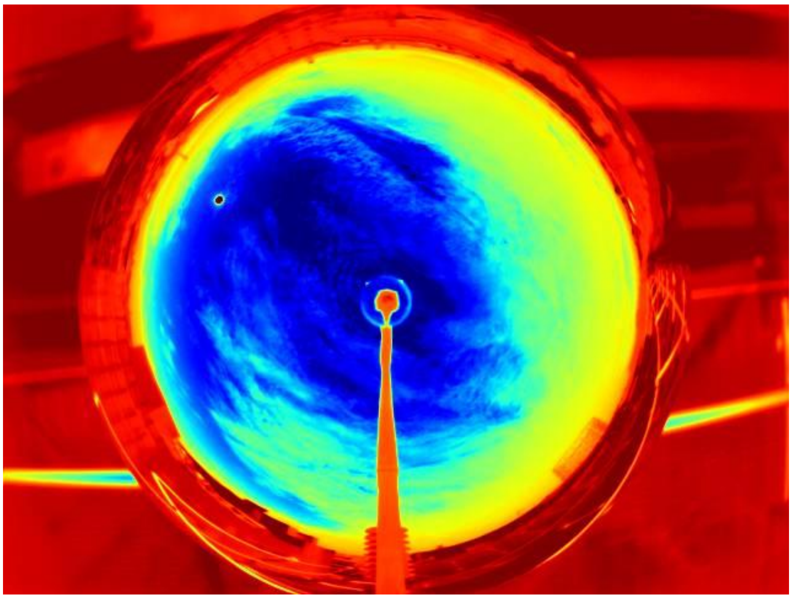

Figure 3. Image acquired on 20 September 2019 at 10.05 a.m.: the blue part is the clear sky, the clouds are represented with different shades and the red that surrounds all the image is the camera system reflection.

Infrared images can be interpreted by referring at the 3D representation in real cardinal coordinates reported in Figure 4.

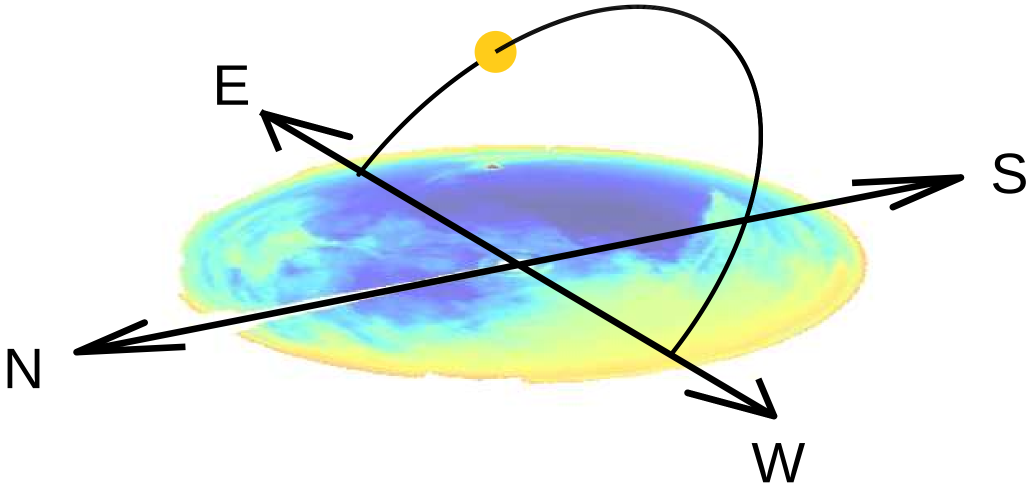

Figure 4. Cardinal coordinates of each image with sun trajectory: it rises to the left, reaches the noon on the top and sets to the right of 2D image.

As models output, the solar attenuation due to the clouds passage is selected since this phenomenon is representative of the PV power fluctuations. There are two possible types of output: an absolute GHI and a relative GHI, expressed through the Clear Sky Index (CSI). This latter parameter, as shown in Equation (1), is derived as the ratio between the measured GHI and the GHI in clear sky conditions in the time interval t, computed through physical modeling accounting for the Sun angles. Clear Sky Index (CSI) is employed due to its several advantages:

- It is not affected by the seasonal fluctuation of solar radiation along the year, being a ratio among solar parameters.
- It is strictly related to the Global Irradiance on the plane of the array and to the output power of the PV plant.
- It is easy to calculate its components, both because GHIcs is deterministic and because GHIm could be easily measured especially in complex building conditions when the PV system is made by arrays of PV modules with different tilt and azimuth.

$$CSI\big|_t = \frac{GHI_m\big|_t}{GHI_{cs}\big|_t} \tag{1}$$

The absolute value of GHI is directly comparable with the PV power production, but it presents a non-negligible dependence on the period of the year and on the moment of the day. Therefore, its variation in the time horizon of few minutes is influenced even by parameters other than the cloud cover. Considering the time period corresponding to the available data, indeed, irradiance values recorded in different seasons exhibit large variability. On the other hand, the CSI allows to remove the diurnal and seasonal effects typical of absolute GHI and, therefore, it reflects the irradiance variability related to the only cloud cover. In light of that, this indicator is more suitable than the absolute GHI to provide a general overview starting from data covering large time spans and, therefore, it is selected as output of the models.

The CSI output is not a specific value, but a class corresponding to a range of possible values. In more detail, five output classes are defined through strict threshold values reported in the Table 2. These five classes are partially related to previous works of the same authors [32,33] where, at first, three-day types are included: "cloudy", "partially cloudy" and "clear" days. However, when dealing with the clear sky index for classification purposes, in the literature there are different thresholds and these could strongly depend on the typical weather conditions related to the given location [34,35] (i.e., desertic areas, rainy forests, etc. …). In this study case, a linear partition to five classes is a reasonable compromise between too many classes scarcely populated and few overcrowded. Moreover, this five-classes partition allows detecting more dense sudden changes in solar radiation variations. The chart in Figure 5 expresses the number of samples in each class. To have a lower number of samples in a particular class is a common issue in classification problems, and sometimes either a different data grouping criteria or merging different classes together could be a possible solution. In this work, class 5, even if with a reduced number of samples, is kept separated from the others to spot those weather conditions with "over-irradiance" which are not statistically significant (class 5 samples account 4% of the times), but which could highlight particular operating conditions in the PV system (i.e., with solar irradiance higher than Standard Test Conditions). To have meaningful prediction of this class, it is reasonable to assume that an equal share among data classes, in terms of equal number of samples, should be employed and the lack of this homogeneity in our case study is slightly affecting the classification results, in particular when considering class 5 samples.

Table 2. Range of CSI values for each class.

Classes	CSI Values	Sky Conditions
1	$(0; 0.2]$	Overcast
2	$(0.2; 0.45]$	Partially cloudy
3	$(0.45; 0.75]$	Partially cloudy
4	$(0.75; 1]$	Clear sky
5	$(1; 1.6]$	Over-irradiance

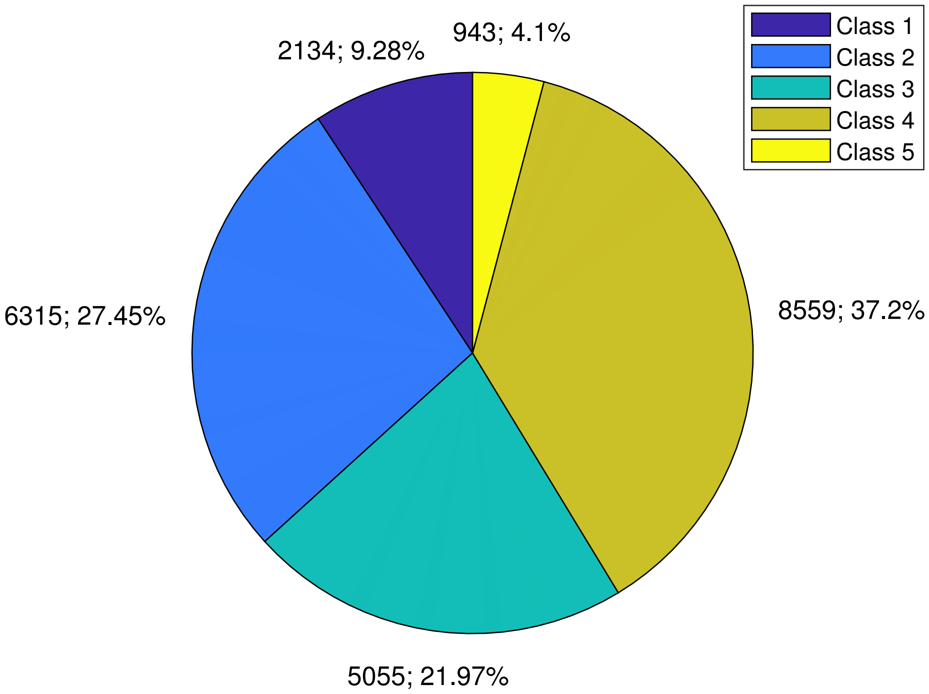

Figure 5. Amount of samples in the five CSI classes with the relevant share of the available data.

In the present work, CSI is not only an output parameter, but it is exploited also as input: CSI value at time T is provided as input to the model to forecast the CSI class at time $T + \Delta T$, where ΔT is the time horizon.

Concerning the other input parameters, several features are extracted from the infrared images. The following list contains all the features computed for each of the available sky images:

- σ_S: standard deviation of the pixel values in a small circular crown around the sun computed separately for the red, green and blue channels.

- μ_s: mean of the pixel values in a small circular crown around the sun computed separately for the red, green and blue channels.
- σ_l: standard deviation of the pixel values in a large circular crown around the sun computed separately for the red, green and blue channels.
- μ_l: mean of the pixel values in a large circular crown around the sun computed separately for the red, green and blue channels.

Other than those features, additional information about GHI and solar angles, such as solar elevation (α) and azimuth (ψ), are exploited during classification.

In general, the model development can be improved by training it with data about the dynamic behavior of the system, namely, information about its previous states: for this reason, as predictors, all parameters in the 3 min before the time T_0 (except for solar angles) are provided to the model to forecast the CSI class at time $T_0 + \Delta T$. The general prediction scheme is depicted in Figure 6.

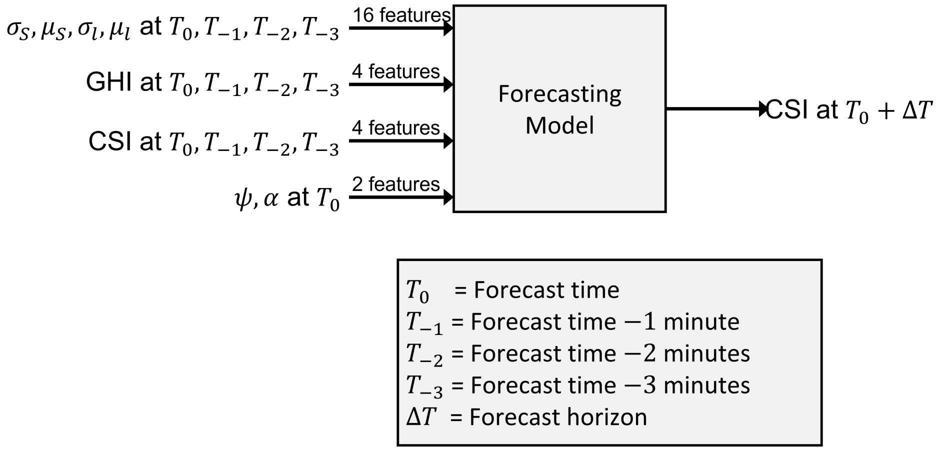

Figure 6. Prediction scheme for all the proposed models.

Once all data are stored, they undergo a proper cleaning procedure: it is necessary to remove all the inconsistent samples and samples with missing values, in order to avoid their potential negative influence on the forecast models performance. Moreover, all samples related to rainy days (selected through the use of rain gauge) are excluded from training since the presence of droplets on the mirror surface hinders a proper calculation of the input parameters starting from the infrared images.

2.3. Evaluation Metrics

The performance evaluation is a crucial step to assess the capability of the model to correctly identify the CSI class to whom an unlabeled sample belongs. All the classification models, regardless of the underlying algorithm and the forecast horizon, are developed starting from a common input dataset and their performances are evaluated on the basis of common evaluation metrics.

Specifically, four metrics are considered: accuracy, precision, recall and F1 score for each CSI class. The first three metrics are derived from the confusion matrix, while the last can be calculated as a proper combination of the others.

The test accuracy provides an overview of "how well" a model is doing, returning the fraction of predictions the model got right. Considering a generic day d, the daily accuracy (A_d) is calculated as stated in Equation (2).

$$A_d = \frac{TP_d}{N_d} \tag{2}$$

where TP_d (True Positives) is the number of samples in day d correctly classified by the model, while N_d is the number of available samples in day d. In larger time periods, the overall accuracy (A) is simply computed by averaging the daily values, as in Equation (3).

$$A = \frac{\sum_1^N A\_d}{N} \tag{3}$$

where N is the number of days in the considered time period.

The precision (P), also denoted as "positive predictive value", for a class C is calculated as stated in Equation (4). It defines how trustworthy an outcome is when the model associates a sample to a specific class.

$$P = \frac{TP}{TP + FP} \tag{4}$$

where TP is the number of samples that the model correctly classifies, namely, those truly belonging to class C; FP (False Positives) is the number of samples that the model incorrectly classifies as belonging to class C, while they belong to a different class.

The recall (R), also denoted as "sensitivity", for a class C expresses how well the model is able to detect that class. It is calculated as stated in Equation (5).

$$R = \frac{TP}{TP + FN} \tag{5}$$

where TP is the number of samples that the model correctly classifies, namely, those truly belonging to class C; FN (False Negatives) is the number of samples belonging to class C that are incorrectly classified as belonging to a different class.

Considering a specific class C, one the following situations occurs:

- In the case that C is accurately recognized by the model, both high recall and high precision are observed.
- In the case that C is not well recognized by the model but, when recognized, the outcome is reliable, low recall and high precision are observed.
- In the case that C is well recognized but the model assigns to C also points from other classes, high recall and low precision are observed.
- In the case that C is poorly recognized by the model, both low recall and low precision are observed.

The F1 Score ($F1$) combines precision and recall in one single metric. In detail, it consists of the harmonic mean of their value, as stated in the Equation (6). Whereas the arithmetic mean equally weights all values, the harmonic mean assigns larger weight to low values. As for precision and recall, this metric is also defined for a specific class C.

$$F1 = 2 \cdot \frac{P \cdot R}{(P + R)} \tag{6}$$

3. Results

The classification performances reported in the current chapter are computed on the available data previously described.

3.1. Model Definition

The ANN and the RF methods are characterized by some important parameters that highly affect the performances of the method. In particular, for the ANN, the number of neurons in the hidden layer is the key feature that should be analyzed; for the RF, it is the number of trees. Both these parameters can be found heuristically with a sensitivity analysis.

The sensitivity analysis on the neural network size has been performed training 15 independent times the network in order to reduce the impact of the stochastic weight initialization. In addition, for each of the 15 trials, the dataset splitting between training, validation and testing has been resampled randomly. The optimal size of the ANN is determined by the number of hidden neurons above which the improvement is negligible.

This analysis has been performed on all the identified time horizons (from 1 to 5 min). Figure 7 shows the results obtained with time horizon equal to 5 min. The complete results for all the time horizons are summarized in Table 3.

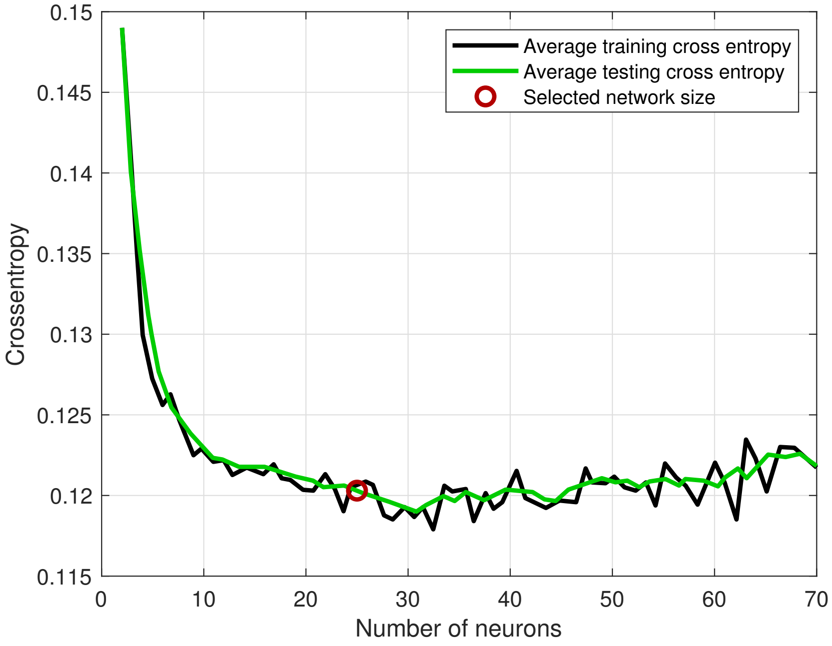

Figure 7. Sensitivity analysis on the number of neurons in the ANN with time horizon equal to 5 min.

Table 3. Results of the sensitivity analysis on the ANN hidden layer.

Time horizon	TH1	TH2	TH3	TH4	TH5
Optimal number of neurons	13	16	20	23	25

A sensitivity analysis on the number of trees has been performed for the RS model. In this case, the performance has been computed with the out-of-bag algorithm, which is capable of avoiding the lack of generalization. The results of this analysis for the time horizon equal to 5 min are shown in Figure 8. The results on all the time horizons are reported in Table 4.

Table 4. Results of the sensitivity analysis on the RF number of trees.

Time horizon	TH1	TH2	TH3	TH4	TH5
Optimal number of trees	114	92	116	167	153

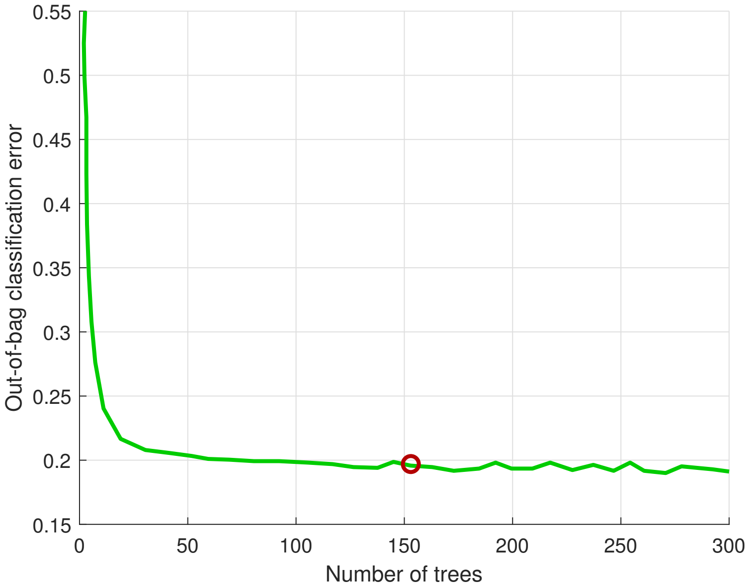

Figure 8. Sensitivity analysis on the number of trees in the RF with time horizon equal to 5 min.

3.2. Models Comparison

First, a performance evaluation is carried out comparing the two proposed classification algorithms by means of the previously defined evaluation metrics and in function of the different forecast horizons considered. The summary in Table 5 refers to the ANN performance and contains each index calculated and the percentage differences (Δ) between cases with time horizon of 1 min (TH1) and 5 min (TH5). The five classes are indicated with names from C1 to C5.

Table 5. Indexes of performance for ANN model.

		TH1	**TH2**	**TH3**	**TH4**	**TH5**	**Δ**
A (%)		87.7	83.6	80.3	77.8	76.4	11.3
P (%)	**C1**	95.9	93.2	92.5	91.5	90.3	5.6
	C2	93.5	90.3	86.3	85.7	83.6	9.9
	C3	83.9	74.8	76.8	68.7	68.6	15.2
	C4	88.4	87.9	84.4	84.9	79.7	8.7
	C5	78.6	66.7	64.7	60.8	62.4	16.2
R (%)	**C1**	97.4	96.3	92.8	92.7	91.3	6.1
	C2	92.0	87.6	86.7	83.5	81.3	10.7
	C3	79.3	77.6	70.6	72.2	65.2	14.1
	C4	93.1	89.3	89.9	87.0	88.0	5.1
	C5	69.1	51.9	52.4	38.6	30.7	38.4
F1 (%)	**C1**	96.6	94.7	92.6	92.1	90.8	5.8
	C2	92.8	88.9	86.5	84.6	82.5	10.3
	C3	81.5	76.2	73.6	70.4	66.9	14.6
	C4	90.7	88.6	87.0	85.9	83.6	7.0
	C5	73.5	58.3	57.9	47.2	41.1	32.4

It is observed that the classification performance, according to all the evaluation metrics considered, worsens when the time horizon increases: indeed, the problem to solve becomes more complicated and difficult to predict. Moreover, performances on some classes suffer greater percentage loss with respect to others according to the class-specific indexes, in particular classes 2, 3 and 5. This can be due to the fact that class 2 and 3 are representative of partially cloudy conditions and, thus, they are the most difficult to identify.

On the other hand, class 5 contains less samples than the other classes, and therefore the capability of the models to recognize this class is lower.

Table 6 summarizes the RF performance. As before, it contains each index calculated and the percentage differences (Δ) between cases with time horizon of 1 min (TH1) and 5 min (TH5) and the five classes are indicated with names from C1 to C5.

Table 6. Indexes of performance for RF model.

		TH1	**TH2**	**TH3**	**TH4**	**TH5**	**Δ**
A (%)		88.4	84.1	80.9	78.1	76.2	12.2
P (%)	**C1**	97.9	96.8	95.7	94.8	93.8	4.2
	C2	93.2	89.8	86.8	85.7	84.5	8.7
	C3	82.2	77.1	73.8	72.5	71.2	11.0
	C4	89.2	86.2	84.6	83.2	82.6	6.6
	C5	76.9	71.3	69.8	69.1	69.6	7.4
R (%)	**C1**	97.7	95.8	94.2	93.0	92.0	5.7
	C2	93.6	90.1	87.6	85.9	84.3	9.3
	C3	81.2	75.6	72.1	70.5	69.3	11.9
	C4	91.5	89.6	88.5	88.0	88.0	3.4
	C5	63.1	53.7	47.6	44.7	42.6	20.5
F1 (%)	**C1**	97.8	96.3	95.0	93.9	92.9	4.9
	C2	93.4	89.9	87.2	85.8	84.4	9.0
	C3	81.7	76.4	72.9	71.5	70.2	11.5
	C4	90.3	87.8	86.5	85.6	85.2	5.1
	C5	69.4	61.3	56.6	54.2	52.9	16.5

It is observed that the RF model has the least loss of performance by increasing the time horizon in terms of precision, recall and F1 score. On the contrary, the performance loss in terms of accuracy is slightly lower with the ANN classifier. All methods perform similarly on all the considered forecast horizons. In general, the RF slightly outperform the ANN except for the time horizon TH5, where the ANN is the best performing classifier.

3.3. Performance Evaluation on Specific Days

An additional analysis is performed on four days with at least one sample for each CSI class where the classification models developed present the best and the poorest performances considering a time horizon of 5 min. The dates 27 September 2019 (Figure 9) and 5 November 2019 (Figure 10) constitute the days where the ANN presents, respectively, the best and the worst classification performance. On the other hand, 3 March 2020 (Figure 11) and 15 March 2020 (Figure 12) represent the days where the RF presents, respectively, the best and the worst classification performance.

Figures 9–12 report the trend of CSI in the considered days and highlight the borders of the different CSI classes. Additional information provided is related to the relevance of the classification errors committed by the classification models on specific time frames. A "less relevant incorrect classification" is a classification error that associates a time sample to a CSI class which is contiguous to its real one. On the contrary, a "most relevant incorrect classification" is a classification error that associates a time sample to a CSI class which is not contiguous to its real one, estimating an irradiance level which is largely different from the observed one.

A common characteristic between days characterized by bad classification performances is the sudden variability in CSI value, fluctuating between different classes in short time intervals. On the contrary, on days characterized by accurate classification performances, the changes in solar irradiation are more gradual and the CSI trend is less rugged.

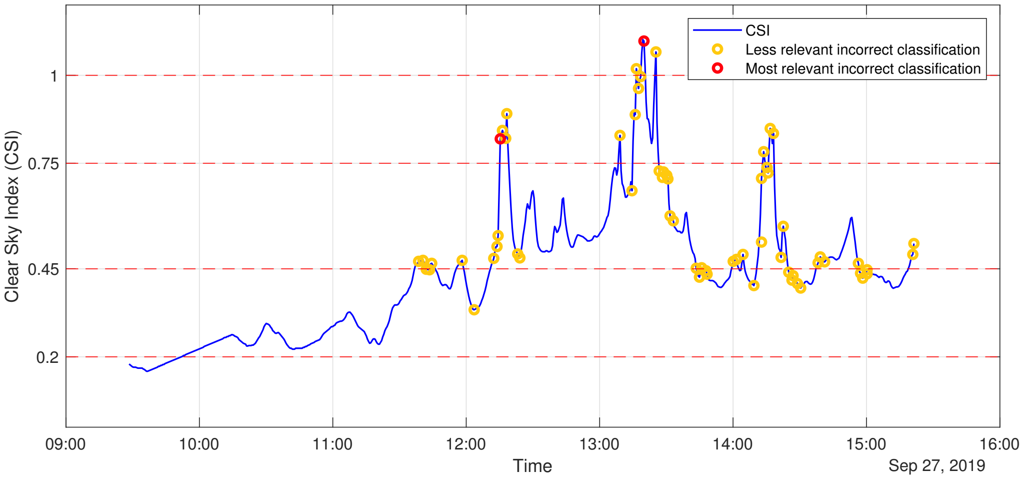

Figure 9. CSI trend with highlighted classification errors for the day of 27 September 2019.

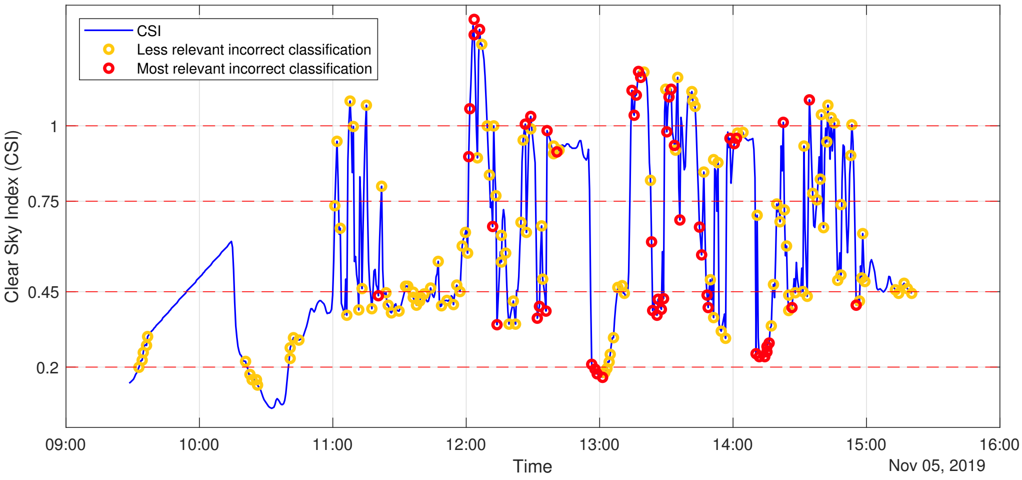

Figure 10. CSI trend with highlighted classification errors for the day of 5 November 2019.

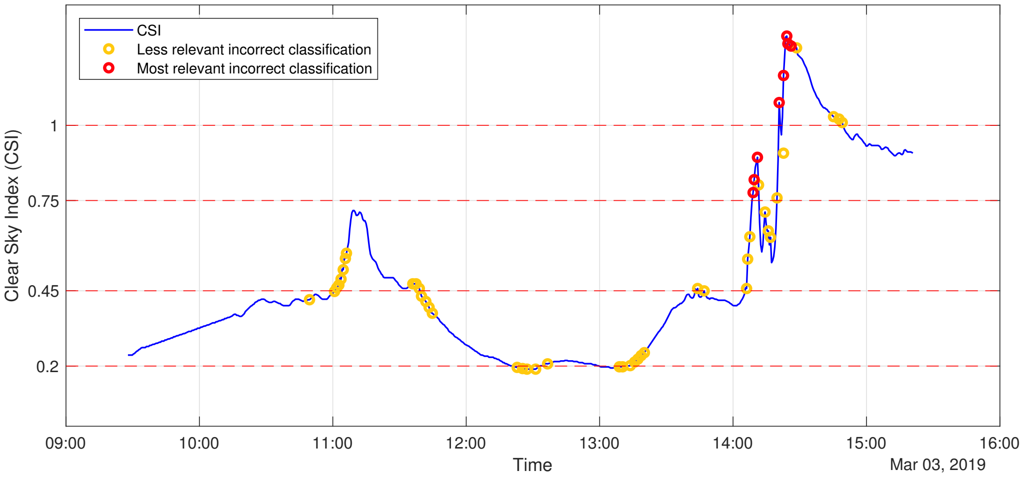

Figure 11. CSI trend with highlighted classification errors for the day of 3 March 2020.

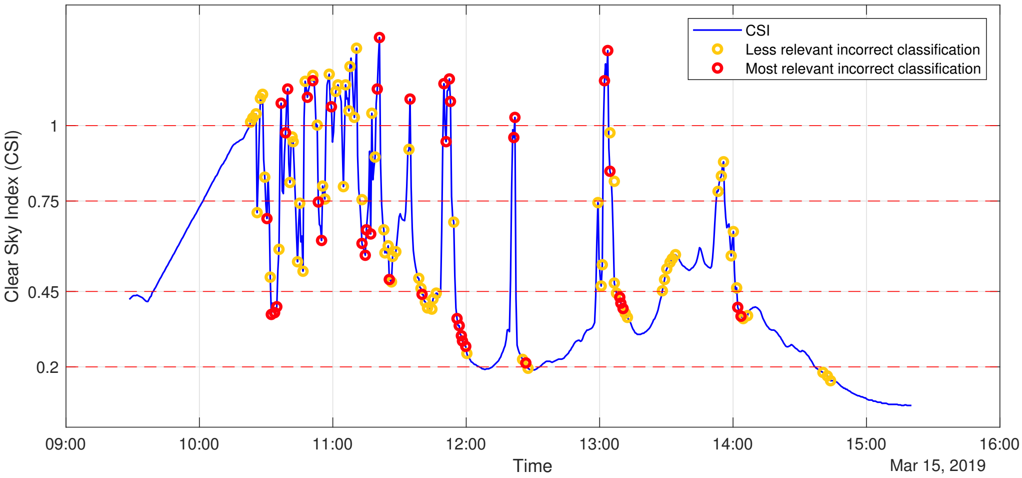

Figure 12. CSI trend with highlighted classification errors for the day of 15 March 2020.

Table 7 shows the CSI classes numerosity for each day and the test accuracy achieved by each method.

Table 7. Performance and class composition of the days selected for the performance comparison.

	Number of Samples					Test Accuracy	
Day	**C1**	**C2**	**C3**	**C4**	**C5**	**ANN**	**RF**
27 September	10	185	118	16	3	79.8%	74.4%
5 November	23	117	82	75	35	42.5%	62.8%
3 March	8	200	54	41	29	77.4%	81.9%
15 March	44	150	71	31	36	63.3%	62.7%

Analyzing the results, it is possible to notice that 5 November is a very critical day due to the large number of high frequency fluctuations in solar irradiance. In addition, another criticality of this day is related to the fact that many samples have a irradiance value very close to the selected limits of the classes. The forecasting accuracy in these cases can be increased by exploiting ensemble forecasting or fuzzy logic.

4. Conclusions

The increasing penetration of PV power systems into the electric grid is leading to the necessity to smooth the PV power fluctuations, related to the intermittency which characterizes the solar source. This task is typically addressed by exploiting battery energy storage systems, whose control logic can be improved by integrating specific forecasting tools capable of estimating the solar irradiance fluctuations in the near future. This control strategy allows to charge and discharge the battery in advance in order to successfully handle peaks and drops in PV power production. Moreover, the integration of a forecasting tool potentially permits to undersize the energy storage capacity, allowing money savings.

The present work proposes two different nowcasting methods capable to predict, over different time horizons ranging from 1 to 5 min, the occurrence of PV power fluctuations: an Artificial Neural Network and a Random Forest model. From the results presented, the following conclusions are drawn:

- From a general perspective, the two proposed models present similar classification performances on all the five time horizons analyzed. Therefore, the proposed nowcasting strategy, aimed at predicting the occurrence of PV power fluctuations on the basis of the combination between infrared sky images and meteorological parameters, performs similarly adopting either ANN or RF classification model. However, in the

presented case study, RF scored the best results both in terms of overall classification accuracy and computational load.
- From a detailed analysis on specific days, it is observed that classification models present reasonable performance whenever the CSI variation is gradual, while their accuracy drops in conditions characterized by sudden solar irradiance fluctuations.

The forecasting time horizon used in this work ranges from 1 min to 5 min; these horizons are valuable when dealing with grid management and with the need of exploiting batteries to smooth power variations.

Finally, the topic discussed presents several potential future developments. One of the main limits related to the proposed irradiance forecasting strategy is related to the strict thresholds imposed to divide the registered CSI values in classes. Thus, it may be worth increasing class number or trying different threshold values, in order to achieve a more convenient and homogeneous class partitioning. Another possible investigation is related to the extracted features: different image features can be tested and specific selection criteria can be applied in order to reduce the dimensionality of the training data. Moreover, classification methods other than ANN and RF, already applied, can be investigated.

Author Contributions: Conceptualization, E.O. and A.N. (Alessandro Niccolai); methodology, A.N. (Alessandro Niccolai); software, V.V.; validation, A.N. (Alessandro Niccolai), A.N. (Alfredo Nespoli) and E.O.; formal analysis, A.N. (Alfredo Nespoli); investigation, E.O.; resources, A.N. (Alessandro Niccolai); data curation, A.N. (Alfredo Nespoli); writing—original draft preparation, V.V.; writing—review and editing, A.N. (Alfredo Nespoli); visualization, E.O.; supervision, R.Z.; project administration, R.Z. All authors have read and agreed to the published version of the manuscript.

Funding: This research received no external funding.

Institutional Review Board Statement: Not applicable.

Informed Consent Statement: Not applicable.

Data Availability Statement: Not applicable.

Conflicts of Interest: The authors declare no conflict of interest.

References

1. Cao, D.; Zhao, J.; Hu, W.; Ding, F.; Huang, Q.; Chen, Z.; Blaabjerg, F. Data-Driven Multi-Agent Deep Reinforcement Learning for Distribution System Decentralized Voltage Control With High Penetration of PVs. *IEEE Trans. Smart Grid* **2021**, *12*, 4137–4150. [CrossRef]
2. Brahma, B.; Wadhvani, R. Solar Irradiance Forecasting Based on Deep Learning Methodologies and Multi-Site Data. *Symmetry* **2020**, *12*, 1830. [CrossRef]
3. Jang, H.S.; Bae, K.Y.; Park, H.; Sung, D.K. Solar Power Prediction Based on Satellite Images and Support Vector Machine. *IEEE Trans. Sustain. Energy* **2016**, *7*, 1255–1263. [CrossRef]
4. Pan, K.; Xie, C.; Lai, C.S.; Wang, D.; Lai, L.L. Photovoltaic Output Power Estimation and Baseline Prediction Approach for a Residential Distribution Network with Behind-the-Meter Systems. *Forecasting* **2020**, *2*, 470–487. [CrossRef]
5. Wang, F.; Lu, X.; Mei, S.; Su, Y.; Zhen, Z.; Zou, Z.; Zhang, X.; Yin, R.; Duić, N.; Shafie-khah, M.; et al. A satellite image data based ultra-short-term solar PV power forecasting method considering cloud information from neighboring plant. *Energy* **2022**, *238*, 121946. [CrossRef]
6. Ahmed, R.; Sreeram, V.; Mishra, Y.; Arif, M.D. A review and evaluation of the state-of-the-art in PV solar power forecasting: Techniques and optimization. *Renew. Sustain. Energy Rev.* **2020**, *124*, 109792. [CrossRef]
7. Elalani, O.; Ghennioui, H.; Ghennioui, A. Intra-day Variability Quantification from Ground-Based Measurements of Global Solar Irradiance. *Generations* **2020**, *10*, 12.
8. Zhu, W.; Zhang, L.; Yang, M.; Wang, B. Solar Power Ramp Event Forewarning with Limited Historical Observations. *IEEE Trans. Ind. Appl.* **2019**, *55*, 5621–5630. [CrossRef]
9. Zhen, Z.; Liu, J.; Zhang, Z.; Wang, F.; Chai, H.; Yu, Y.; Lu, X.; Wang, T.; Lin, Y. Deep Learning Based Surface Irradiance Mapping Model for Solar PV Power Forecasting Using Sky Image. *IEEE Trans. Ind. Appl.* **2020**, *56*, 3385–3396. [CrossRef]
10. Wen, H.; Du, Y.; Chen, X.; Lim, E.G.; Wen, H.; Jiang, L.; Xiang, W. Deep learning-based multi-step solar forecasting for PV ramp-rate control using sky imagers. *IEEE Trans. Ind. Inform.* **2020**, *17*, 1397–1406. [CrossRef]
11. Leva, S.; Nespoli, A.; Pretto, S.; Mussetta, M.; Ogliari, E.G.C. PV plant power nowcasting: A real case comparative study with an open access dataset. *IEEE Access* **2020**, *8*, 194428–194440. [CrossRef]

12. Zhang, R.; Ma, H.; Saha, T.K.; Zhou, X. Photovoltaic Nowcasting With Bi-Level Spatio-Temporal Analysis Incorporating Sky Images. *IEEE Trans. Sustain. Energy* **2021**, *12*, 1766–1776. [CrossRef]
13. Chen, X.; Member, S.; Du, Y.; Wen, H. Forecasting-Based Power Ramp-Rate Control strategies for utility scale PV systems. *IEEE Trans. Ind. Electron.* **2019**, *66*, 1862–1871. [CrossRef]
14. Catalina, A.; Alaíz, C.M.; Dorronsoro, J.R. Combining Numerical Weather Predictions and Satellite Data for PV Energy Nowcasting. *IEEE Trans. Sustain. Energy* **2020**, *11*, 1930–1937. [CrossRef]
15. Blaga, R.; Sabadus, A.; Stefu, N.; Dughir, C.; Paulescu, M.; Badescu, V. A current perspective on the accuracy of incoming solar energy forecasting. *Prog. Energy Combust. Sci.* **2019**, *70*, 119–144. [CrossRef]
16. Yang, D.; Kleissl, J.; Gueymard, C.A.; Pedro, H.T.; Coimbra, C.F. History and trends in solar irradiance and PV power forecasting: A preliminary assessment and review using text mining. *Solar Energy* **2018**, *168*, 60–101. [CrossRef]
17. Barbieri, F.; Rajakaruna, S.; Ghosh, A. Very short-term photovoltaic power forecasting with cloud modeling: A review. *Renew. Sustain. Energy Rev.* **2017**, *75*, 242–263. [CrossRef]
18. Wan, X.; Du, J. Cloud classification for ground-based sky image using random forest. International Archives of the Photogrammetry. *Remote. Sens. Spat. Inf. Sci.-ISPRS Arch.* **2020**, *43*, 835–842.
19. Zhen, Z.; Wang, F.; Sun, Y.; Liu, C.; Wang, B.; Lu, J. SVM Based Cloud Classification Model Using Total Sky Images for PV Power Forecasting. In Proceedings of the 2015 IEEE Power & Energy Society Innovative Smart Grid Technologies Conference (ISGT), Washington, DC, USA, 18–20 February 2015.
20. Feng, C.; Zhang, J. SolarNet: A sky image-based deep convolutional neural network for intra-hour solar forecasting. In Proceedings of the 2020 IEEE Power and Energy Society Innovative Smart Grid Technologies Conference, ISGT 2020, Washington, DC, USA, 17–20 February 2020; Volume 204, pp. 71–78.
21. Ronkiewicz, T.; Aleksiejuk-Gawron, J.; Awtoniuk, M.; Kurek, J. Neural modelling of solar radiation variability. *J. Phys. Conf. Ser.* **2021**, *1736*, 012015. [CrossRef]
22. Nespoli, A.; Niccolai, A.; Ogliari, E.; Perego, G.; Collino, E.; Ronzio, D. Machine Learning techniques for solar irradiation nowcasting: Cloud type classification forecast through satellite data and imagery. *Appl. Energy* **2022**, *305*, 117834. [CrossRef]
23. Feng, C.; Zhang, J. SolarNet: A deep convolutional neural network for solar forecasting via sky images. In Proceedings of the 2020 IEEE Power and Energy Society Innovative Smart Grid Technologies Conference, ISGT 2020, Washington, DC, USA, 17–20 February 2020.
24. Lee, J.; Wang, W.; Harrou, F.; Sun, Y. Reliable solar irradiance prediction using ensemble learning-based models: A comparative study. *Energy Convers. Manag.* **2020**, *208*, 112582. [CrossRef]
25. Mathiesen, P.; Kleissl, J. Evaluation of numerical weather prediction for intra-day solar forecasting in the continental United States. *Sol. Energy* **2011**, *85*, 967–977. [CrossRef]
26. Mutavhatsindi, T.; Sigauke, C.; Mbuvha, R. Forecasting Hourly Global Horizontal Solar Irradiance in South Africa Using Machine Learning Models. *IEEE Access* **2020**, *8*, 198872–198885. [CrossRef]
27. Golik, P.; Doetsch, P.; Ney, H. Cross-entropy vs. Squared error training: A theoretical and experimental comparison. In Proceedings of the Annual Conference of the International Speech Communication Association (Interspeech), Lyon, France, 25–28 August 2013; Volume 2, pp. 1756–1760.
28. Lahouar, A.; Mejri, A.; Ben Hadj Slama, J. Importance based selection method for day-ahead photovoltaic power forecast using random forests. In Proceedings of the 2017 International Conference on Green Energy Conversion Systems (GECS), Hammamet, Tunisia, 23–25 March 2017; pp. 1–7.
29. Gong, S.; Wu, X.; Zhang, Z. Fault Diagnosis Method of Photovoltaic Array Based on Random Forest Algorithm. In Proceedings of the 2020 39th Chinese Control Conference (CCC), Shenyang, China, 27–29 July 2020; pp. 4249–4254.
30. Sky Insight, the Infrared All Sky Camera for Continuous Cloud Observation, Reuniwatt, 13 October 2022. Available online: https://reuniwatt.com/en/247-all-sky-observation-sky-insight/ (accessed on 2 December 2022).
31. Niccolai, A.; Nespoli, A. Sun Position Identification in Sky Images for Nowcasting Application. *Forecasting* **2020**, *2*, 488–504. [CrossRef]
32. Leva, S.; Dolara, A.; Grimaccia, F.; Mussetta, M.; Ogliari, E. Analysis and validation of 24 h ahead neural network forecasting of photovoltaic output power. Mathematics and Computers in Simulation. *Math. Comput. Simul.* **2017**, *131*, 88–100. [CrossRef]
33. Aghaei, M.; Dolara, A.; Grimaccia, F.; Leva, S.; Mussetta, M.; Ogliari, E. PV plant planning and operations by neural network analysis and validation. In Proceedings of the 29th European Photovoltaic Solar Energy Conference and Exhibition, Amsterdam, The Netherlands, 22–26 September 2014; Volume 2226, p. 26202624.
34. Udo, S.O. Sky conditions at Ilorin as characterized by clearness index and relative sunshine. *Sol. Energy* **2000**, *69*, 45–53. [CrossRef]
35. Kudish, A.I.; Ianetz, A. Analysis of daily clearness index, global and beam radiation for Beer Sheva, Israel: Partition according to day type and statistical analysis. *Energy Convers. Manag.* **1996**, *37*, 405–416. [CrossRef]